Supplementary Information

Effects of Ce co-doping to the A site of $Sm_{0.5-x}Sr_{0.5}CoO_{3\pm\delta}$ for high performance air electrode of solid oxide reversible cells

Sovann Khan[†,*], Aleksandar Staykov[†], Junko Matsuda[†], Maksymilian Kluczny[†], Kuan-Ting Wu[†], Kakeru Ninomiya[‡], Maiko Nishibori[‡], Jun Tae Song[†,l], Motonori Watanabe[†] Miki Inada[†,l] and Tatsumi Ishihara[†,l,*]

[†]Advanced Energy Conversion Systems Thrust, International Institute for Carbon-Neutral Energy Research, (WPI-I^{2}CNER), Kyushu University, 744 Motooka, Nishi-ku, Fukuoka 819-0395, Japan
[‡]International Center for Synchrotron Radiation Innovation Smart, Tohoku University, Katahira 2-1-1, Aoba-ku, Sendai 980-8577, Japan
[l]Department of Applied Chemistry Faculty of Engineering, Kyushu University 744 Motooka, Nishi-ku, Fukuoka, 819-0395 Japan

*Corresponding authors: khan.sovann.455@m.kyushu-u.ac.jp (S. Khan); ishihara@cstf.kyushu-u.ac.jp (T. Ishihara)

Experimental:

1. Material synthesis:

$La_{0.9}Sr_{0.1}Ga_{0.8}Mg_{0.2}O_{3-\delta}$ (LSGM) was synthesized by solid-state reaction method. Stoichiometric ratio of LSGM, 9.79 g of power was weighted by using La_2O_3 (99.99%, Kishida, Japan), $Sr(CO_3)$ (99.99%, Wako Pure Chemical Industries Co., Ltd, Japan), Ga_2O_3 (99.99%. Wako Pure Chemical Industries Co., Ltd, Japan), MgO (99.9%, Wako Pure Chemical Industries Co., Ltd, Japan). Thus obtained powder precursors were mixed with ethanol by planetary ball-milling (20 zirconia balls, 5-mm diameter) for 12 hours (48 cycles of 15-min run and 5-min rest). Then, LSGM powder was annealed at 1000 ^oC for 6 hours in air.

NiO-Fe_2O_3 (NiFe) composite (Fe:Ni= 1:9 wt.) was prepared by impregnation of $Fe(NO_3).6H_2O$ (99.9%, Wako Pure Chemical Industries Co., Ltd) on NiO (98%, Wako Pure Chemical Industries Co., Ltd, Japan). 10.48 g of NiO and 6.46 g of $Fe(NO_3).6H_2O$ were mixed into 200 mL of de-ionized water by magnetic stirring. Then, this solution was heated up to 553 K until complete evaporation of water. Solid mixtures was fired at 673 K for 2 hours, and annealed at 1473 K for 6 h in air. Obtained NiFe was ball-milled for 12 h to grind the particles. Final NiFe powder was dried in vacuum oven at 393 K for 24 h.

TiO_2 added $Ce_{0.6}La_{0.4}O_{2-\delta}$ (Ti-LDC) was prepared by solid state reaction. 3.8688 g of La_2O_3 (99.99%, Kishida, Japan) and 6.1312 g of CeO_2 (99.99 %, Sigma Aldrich Inc., USA) were mixed by plenary ball mill (10-mm of diameter, 30 balls) at 300 rpm for 3 h. After that, this mixed powder was dried under IR lamp and annealed at 1633 K for 6 h in ambient condition. Next, LDC particles were coated by TiO_2 nanoparticles on by mixing

0.045 g of TiO_2 (P25, Aerosil, Japan) and 8.955 g of LDC using plenary ball milling (40 g of 3-mm balls) at 300 rpm for 3 hours. This mixed powder was dried under IR lamp and annealed at 800 ^oC for 2 hours. Finally, Ti-LDC powder was grinded by pestle and mortar before screen printing.

2. Cell fabrication:

Slurry preparation: Anode, cathode and buffer layer were prepared by screen-printing method. 1 g of electrode materials, 0.06 g of ethyl cellulose (Kishida Chemical Co. Ltd., Japan) and several drops of 3-hydroxy-2,2,4-trimethylpentyl isobutyrate (Tokyo Chemical Industry Co., Ltd., Japan) were mixed with pestle and mortar until formation of slurry.

LSGM pellet electrolyte preparation: 1.5 g of LSGM powder was pelletized by 20-MPa press, and formed 20-mm pellet was conducted cold isostatic press (CIP) under 250 MPa for 30 min. LSGM pellet was sintered at 1773 K for 6 h in air. Dense LSGM pellet was polished until 0.3 mm of thickness, which was used for electrolyte.

3. Characterizations

X-ray absorption measurement

The X-ray absorption fine structure (XAFS) spectra of Ce *K*-edge (40.44 keV) and L_3-edge (5.72 keV) were measured at SPring-8 BL01B1. The powder samples were pressed into pellets with a diameter of 10 mm with boron nitride powder. The XAFS measurements were carried out at room temperature in transmission mode.

STEM observation and electron energy loss spectroscopy (STEM-EELS)

STEM-EELS analysis was performed by using Titan ETEM G2 (FEI, USA) equipped with a GIF Quantum energy filter (Gatan Inc., USA) at an acceleration voltage of 300 kV.

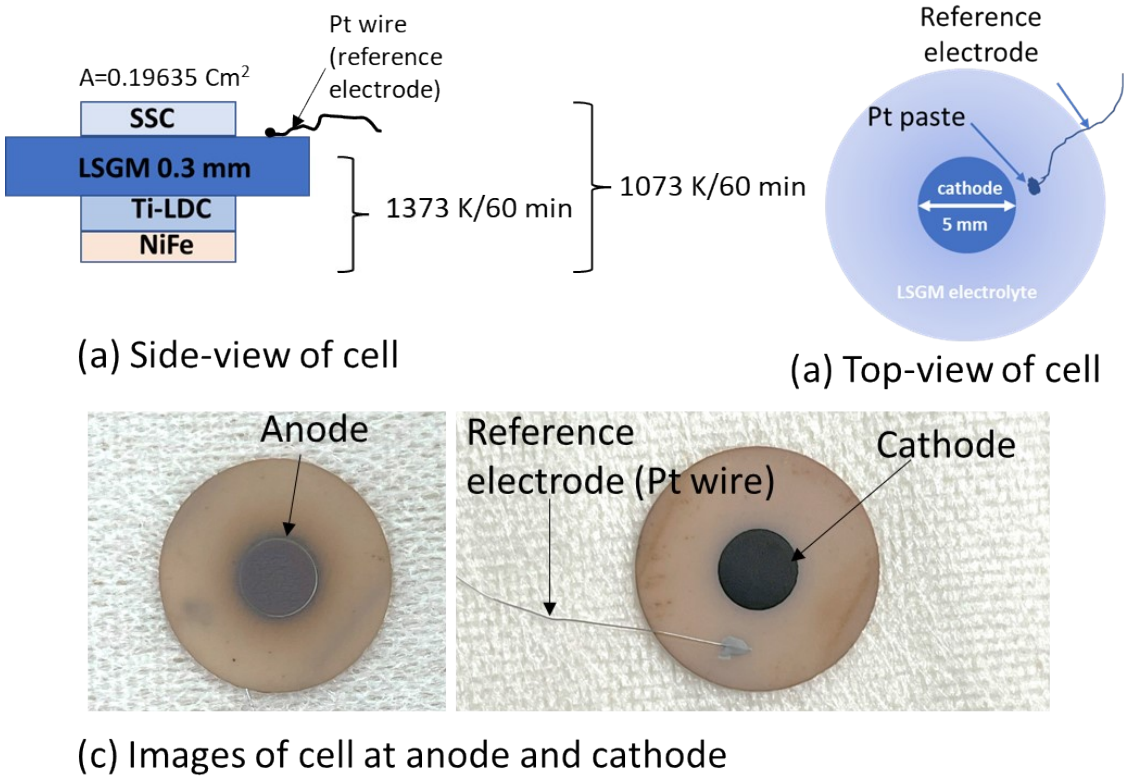

Figure S1: Cell configuration (a) & (b) and photographs of the prepared cell (c)

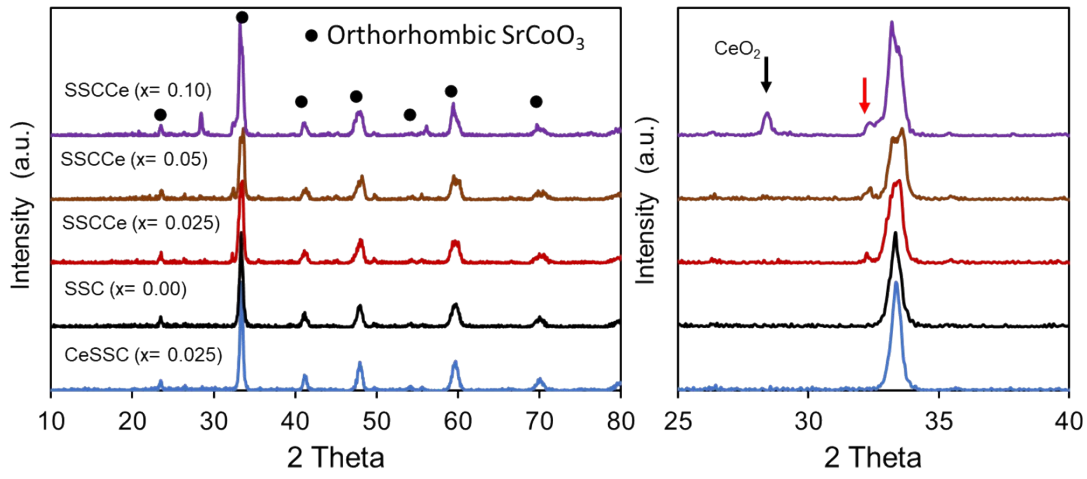

Figure S2 XRD spectra of Ce co-doped at Sr site (CeSSC) and Co-site (SSCCe)

It is different from Sr-site co-doping. Ce co-doping at Co-site possesses binary phases even with a small amount of Ce content (x = 0.025) (see red arrow). Besides the major peaks of orthorhombic structure, the new phase was indexed to tetragonal phase.

Zhang at al. co-doped Ce at Co-site ($Sm_xSr_{1-x}Co_{1-y}Ce_yO_{3-\delta}$) reported that binary or single phase could be obtained in accordance with Sm or Ce co-doping contents [1]. When Ce content is increased to x = 10, CeO_2 phase which is impurity phase is detected.

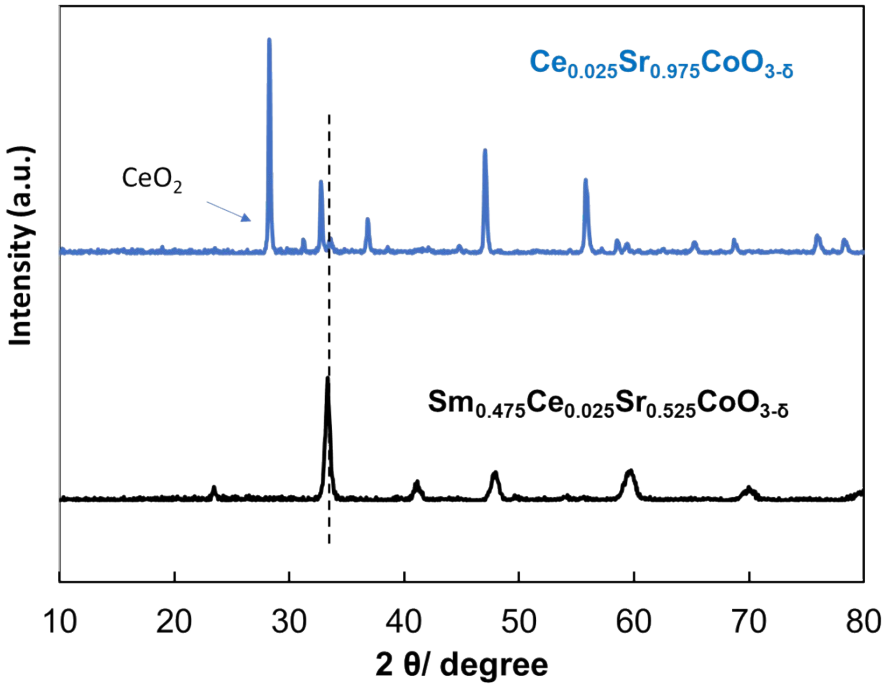

Figure S3 Comparison of XRD patterns of Ce doping at A site with and without Sm-co-doping

Table S1 Elemental composition estimated by EDS analysis and their stoichiometric ratio

Ce, x	EDS (at %)				Stoichiometry (at %)			
	Ce	Sm	Sr	Co	Ce	Sm	Sr	Co
0	0	24.61 (±0.38)	25.57 (±0.86)	49.63 (±0.57)	0	25	25	50
0.025	1.62 (±0.08)	23.65 (±0.33)	25.05 (±0.70)	49.68 (±0.47)	1.25	23.75	25	50
0.05	2.31 (±0.08)	23.57 (±0.21)	24.87 (±0.38)	49.24 (±0.31)	2.5	22.5	25	50
0.10	5.07 (±0.07)	20.17 (±0.25)	25.62 (±0.72)	49.03 (±0.41)	5	20	25	50
0.15	7.78 (±0.16)	17.81 (±0.19)	25.71 (±0.58)	48.70 (±0.38)	7.5	17.5	25	50
0.25	12.04 (±0.25)	12.64 (±0.23)	25.87 (±0.51)	49.45 (±0.60)	12.5	12.5	25	50

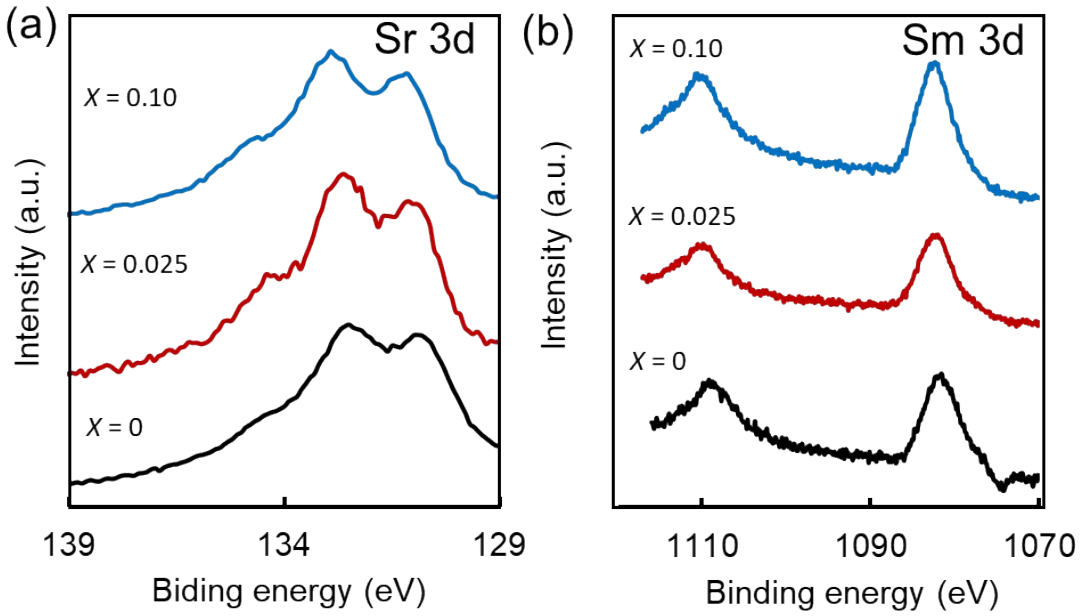

Figure S4 High-resolution XPS spectra of Sr 3d and Sm 3d from samples with different Ce co-doping

Table S2 Atomic ratio of different oxygen species obtaining from XPS deconvoluting peaks

Ce, x	Ce^{3+}/Ce^{4+}	Co^{2+}/Co^{3+}	$O_{chemisorbed}/O_L$
0	-	0.18	0.44
0.025	0.31	0.50	0.30
0.10	0.24	0.60	0.24

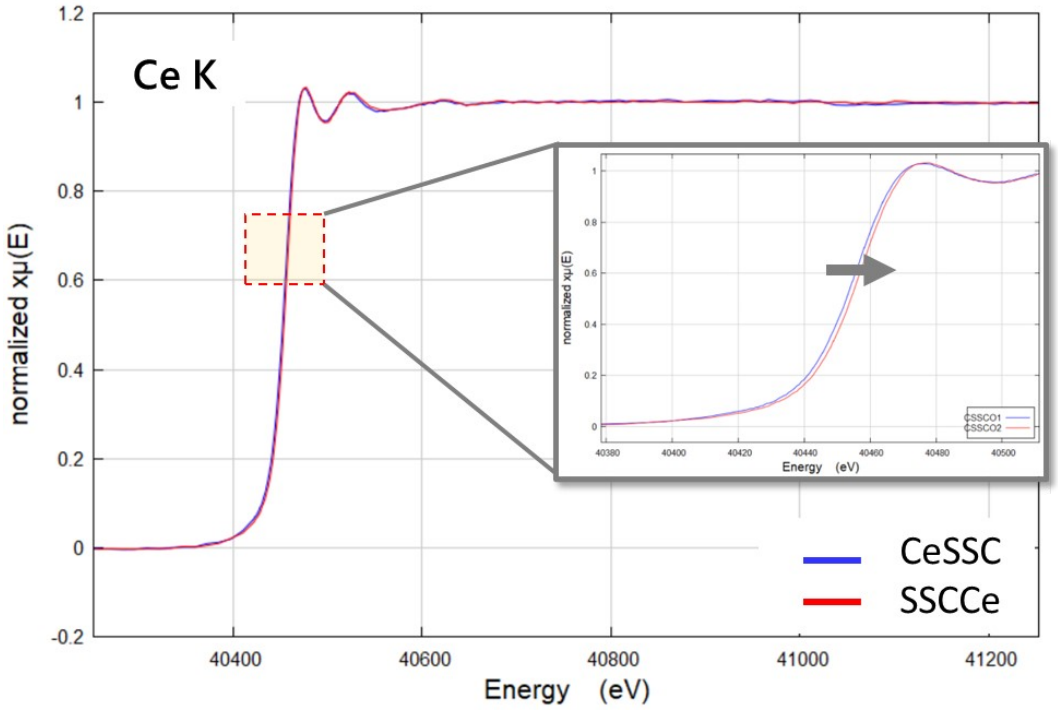

Figure S5 Ce K-edge XAFS spectra of CeSSC and SSCCe

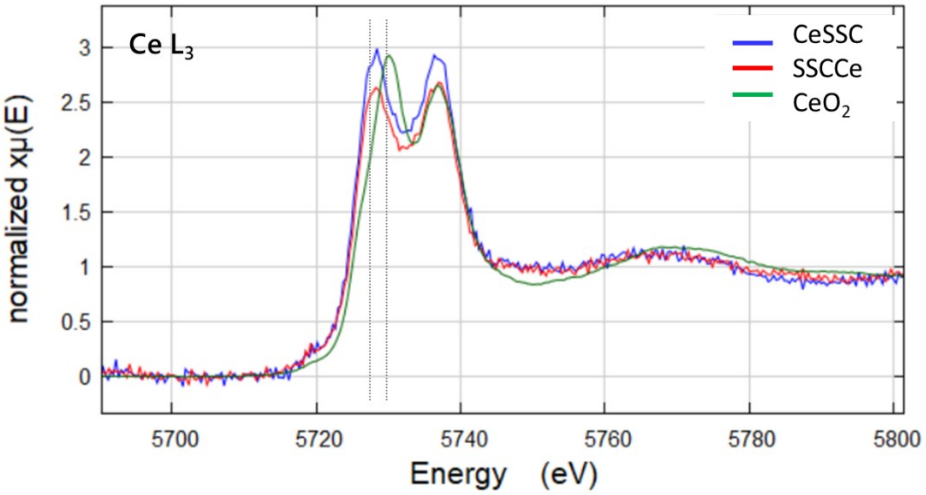

Figure S6 Ce L_3-edge XAFS spectra of CeSSC, SSCCe and CeO_2.

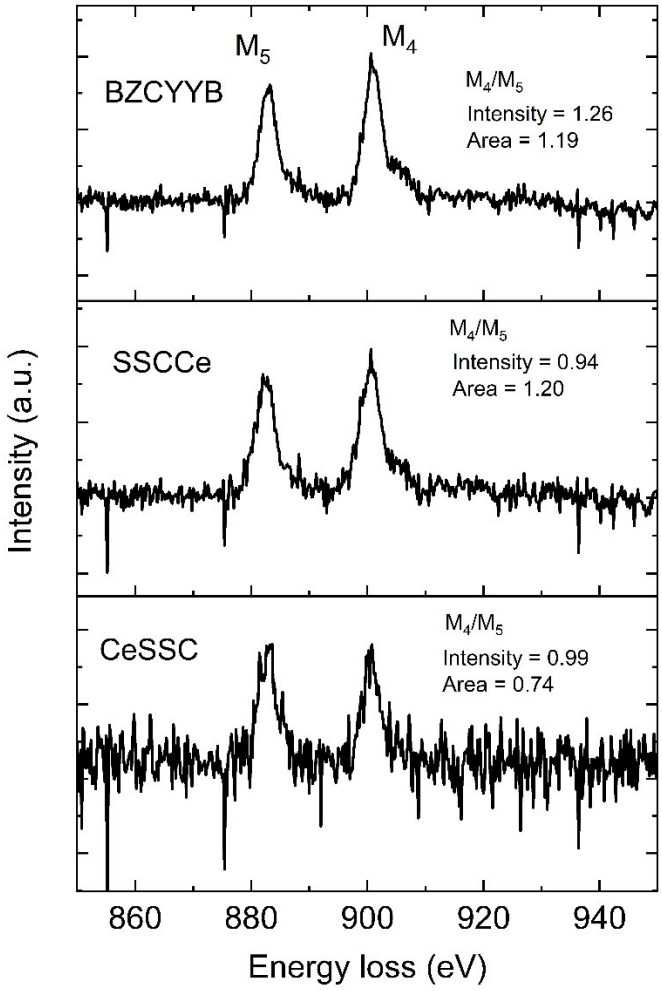

Figure S7 EELS spectra of CeSSC, SSCCe and controlled sample of BZCYYb.

The oxidation state of Ce ions can be characterized by spin-orbit coupling spectra of $3d_{3/2} \rightarrow 4f_{5/2}$ (M_4) and $3d_{3/2} \rightarrow 4f_{7/2}$ (M_5). The ratio of M_4/M_5 peak can be used to identify the valence state of Ce ions. The higher M_4/M_5 ratio indicates the higher valence state of Ce ion [2]. The M_4/M_5 ratio can be varied depending on the calculated methods. In this study, we calculated the ratio of highest intensity and integration area under curves. And, the M_4/M_5 ratio of Ce ion in our samples confirm that mixed valence state of Ce^{3+} and Ce^{4+} exist in as co-dopant in both Sr and Co-site doping. For reference, $BaZr_{0.1}Ce_{0.7}Y_{0.1}Yb_{0.1}O_{3-\delta}$ (BZCY) sample is also analyzed. In BZCYYB sample, Ce is a B-site cation and high oxidation state of Ce^{4+} is dominated. Based on the ratio of M_4/M_5, higher oxidation state of Ce ion is rich in B-site.

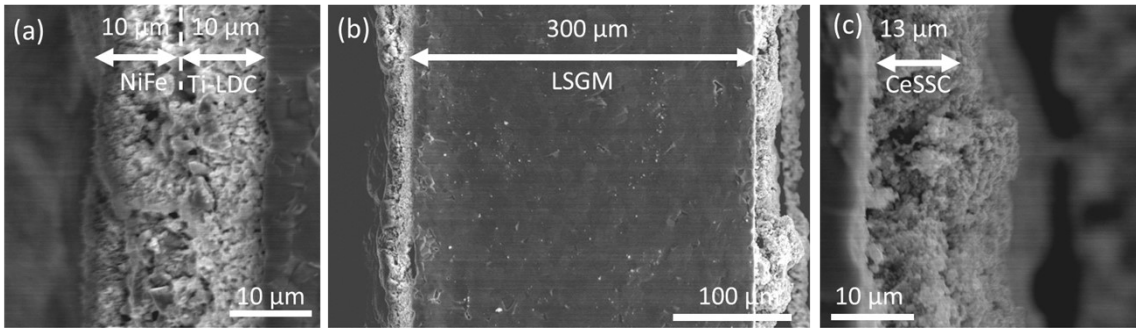

Figure S8 SEM images of cross-section of CeSSC cell after reaction

Cross-sections of the cell after reaction showed that thickness of LSGM electrolyte was ~0.3 mm. And other electrode layers are about 10 µm.

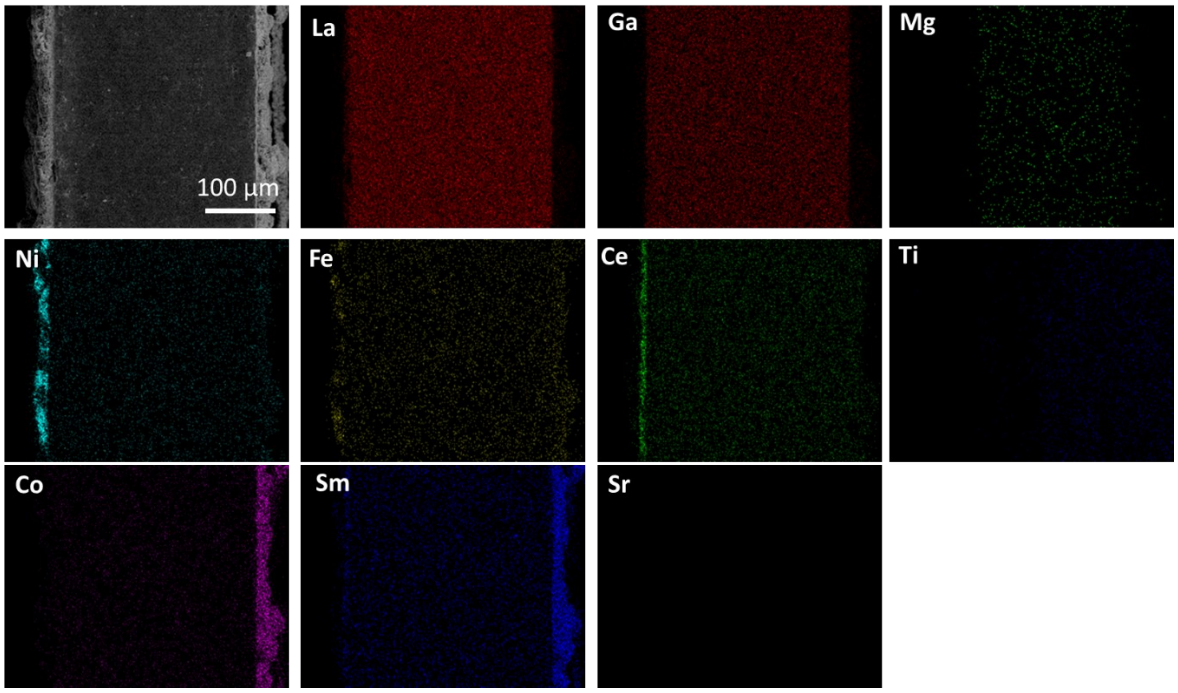

Figure S9 EDS elemental mapping of cross-section of cell after reaction

EDS elemental mapping shows that cell composes of anode (Ni, Fe), buffer layer (Ce, Ti, La), electrolyte (La, Sr, Ga, Mg), and cathode (Co, Sr, Sm, Ce). No elemental diffusion in each component layer were observed

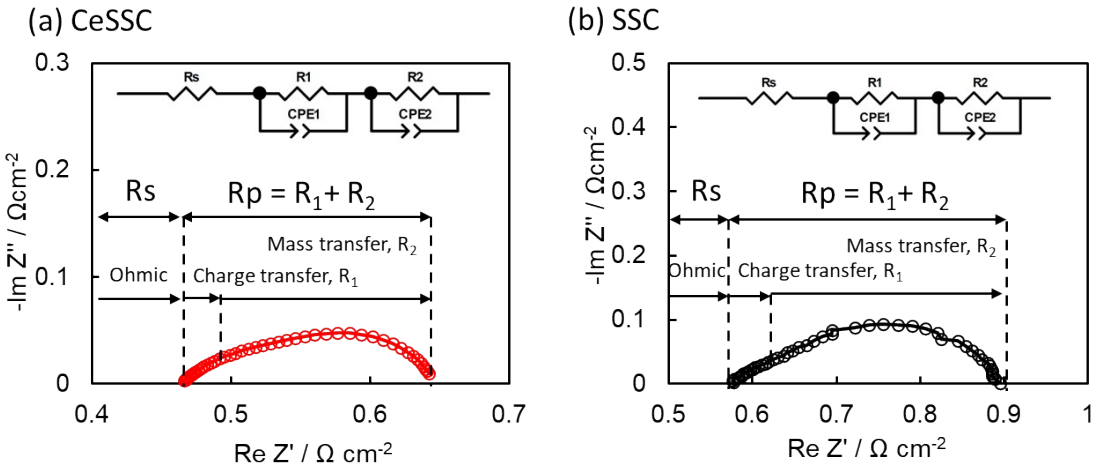

Figure S10 Fitting cuicuits of cells' EIS spectra and their components at 973 K

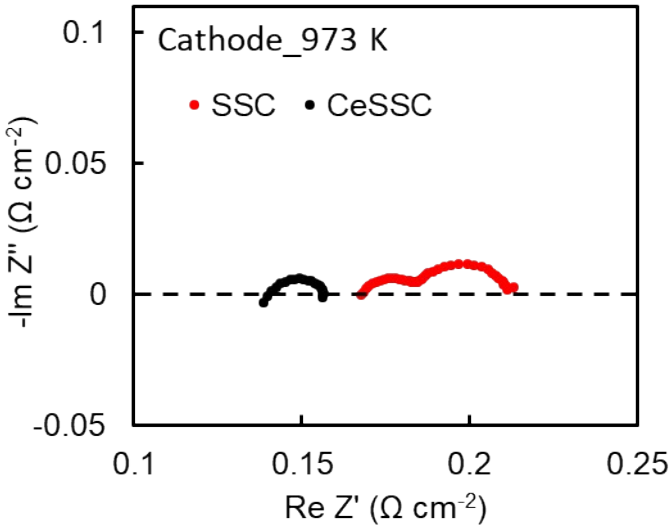

Figure S11 EIS spectra of half-cell of cathode (cathodic impedance) at 973 K

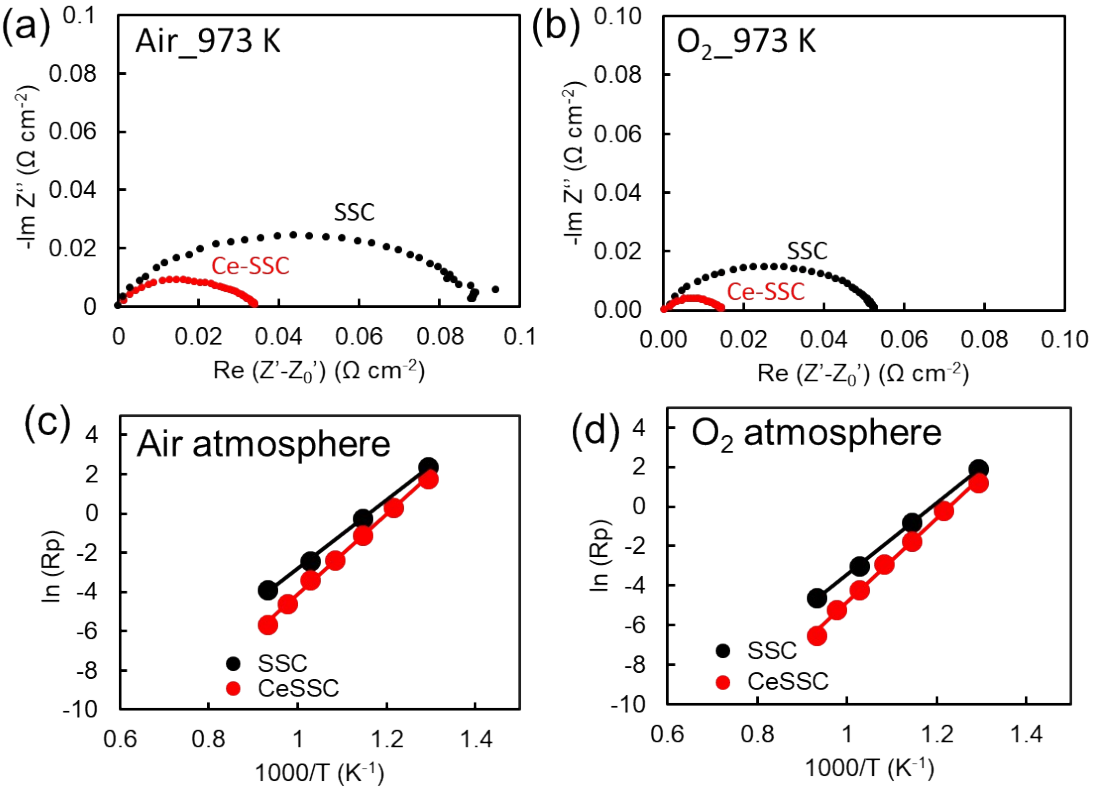

Figure S12 EIS spectra of symmetric cells at 973 K (a) and (b) EIS spectra in air and oxygen atmospheres, (c) and (d) the Arrhenius plots in air and oxygen atmosphere

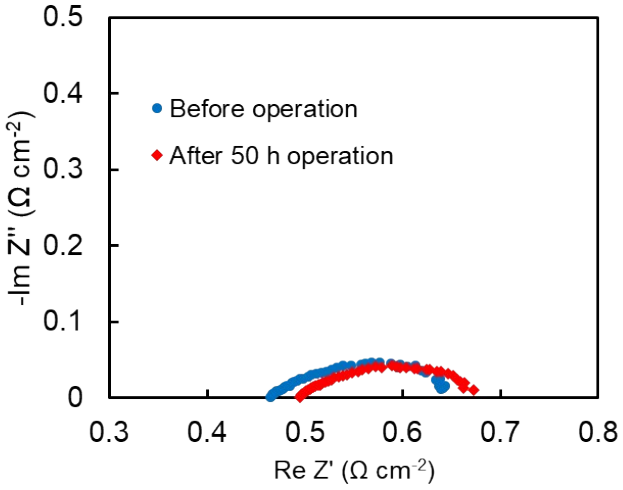

Figure S13: EIS analysis of cell before and after long-term operation at 973 K for 50 h

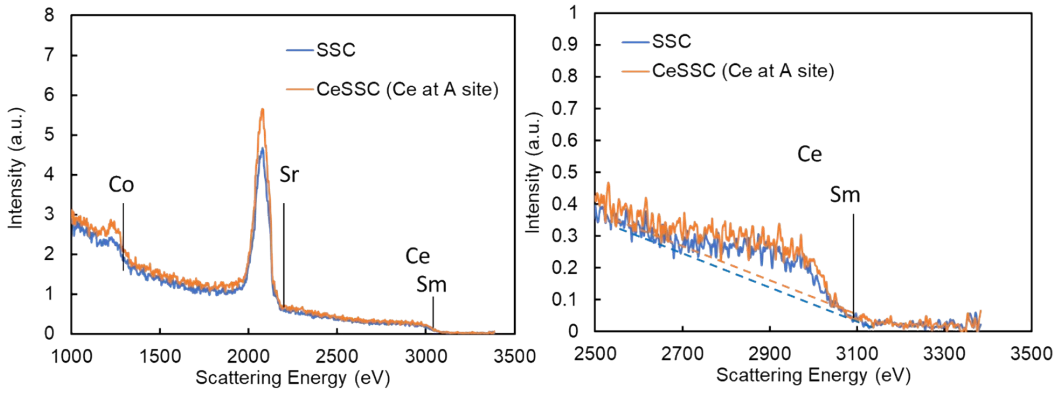

Figure S14 LEIS spectra of SSC and CeSSC

Table S3: Ratio of area under peaks of LEIS spectra

Sample	Co/(Co+Sr+Ce/Sm)	Sr/(Co+Sr+Ce/Sm)	(Ce+Sm)/(Co+Sr+Ce/Sm)
SSC	0.06	0.88	0.06
CeSSC	0.07	0.87	0.06

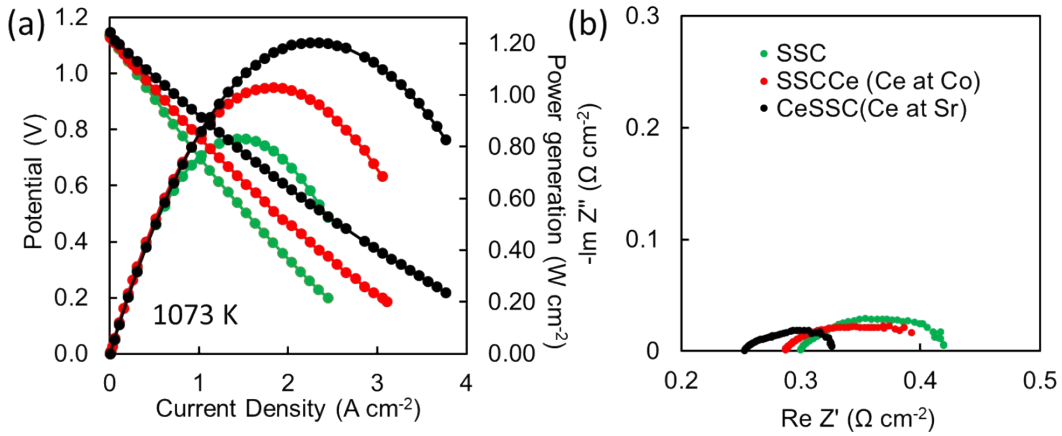

Figure 15: I-V, I-P curves and their EIS spectra of cells made with different cathode materials operated at 1073 K

Table S4 Comparison of FC performance with similar cell performances reported

Anode	Cathode	Electrolyte	Cell structure	Condition	Power (W/Cm^{-2})	Ref.
NiO-$Sm_{0.2}Ce_{0.8}O_{2-\delta}$ (Ni-SDC)	$Sr_{0.9}Ce_xC_oO_{3-\delta}$ (SCCO)	LSGM	NiO-SDC|LDC|LSGM|SCCO	Air/H_2-3%H_2O	0.48 (1073 K)	2015 [3]
Ni-SDC Ni-SDC	$Sr_{0.9}Y_{0.1}CoO_{3-\delta}$ (SYC10) $Sr_{0.9}Y_{0.1}CoO_{3-\delta}$ (SYC10)-GDC	LSGM LSGM	Ni-SDC|LSGM|SYC10 Ni-SDC|LSGM|SYC10-GDC	Air/H_2 Air/H_2	0.64 (1073 K) 0.74 (1073 K)	2020 [4]
NiFe	SSC	LSGM	NiFe|LSGM|SSC	O_2/H_2-3%H_2O	0.80 (1073 K)	2021 [5]
NiO	$La_{0.6}Sr_{0.4}Co_{0.2}Fe_{0.8}O_{3-\delta}$ (LSCF)	SDC/LSGM/SDC	Ni|Ni-SDC|SDC|LSGM|SDC|LSCF-SDC anode-support thin film cell	Air/H_2	1.08 (1073 K) 0.94 (1023 K) 0.74 (973 K)	2022 [6]
$Pr_{0.4}Sr_{0.6}Fe_{0.8}Ni_{0.1}Nb_{0.1}O_{3-\delta}$ (PSFNNb)	LSCF	LSGM	PSFNNb-GDC|LSGM|LSCF-GDC	Air/humid H_2	0.59 (1073 K)	2022 [7]
LSCF	LSCF-GDC	LSGM	LSCF|LSGM|LSCF-GDC	Air/3%H_2O-H_2	0.72 (1073 K) 0.52 (1023 K) 0.31 (973 K)	2022 [8]
Ni-SDC	$La_{1.2}Sr_{0.8}Co_{4-\delta}$ (LSC) nanofibers	LSGM	Ni-SDC|LSGM|LSC	Air/H_2	0.72 (1073 K)	2023 [9]
$La_{0.43}Ca_{0.37}Ti_{0.94}Ni_{0.}06O_{3-\delta}$ (LCTNi)	FSCF	LSGM	LCTNi|LDC|LSGM|LSCF	Air/H_2-3%H_2O	0.43 (1073 K)	2023 [10]
$SrMo_{0.8}Fe_{0.2}O$ (SMF)	$SrCo_{0.5}Fe_{00.45}Ti_{0.05}O_3$ (SCFTi)	LSGM	SMF|LDC|LSGM|SCFTi	Air/H_2	0.46 (1073 K)	2023 [11]
$PrSr(Cu,Fe)_{0.9}Mn_{0.1}O_{4-\delta}$ (RP-PSCFM)/ Cu-Fe (CFA)/GDC	LSFC/DGC	LSGM	RP-PSCFM-CFA-GDC|LSGM|LSCF-GDC	Air/3%H_2O-H_2	1.00 (1073 K) 0.68 (1023 K) 0.41 (973 K)	2023 [12]
$Sr_2Fe_{1.5}Mo_{0.5}O_{6-\delta}$(SFM)/GDC	$Pr_{0.2}Ba_{0.2}Sr_{0.2}La_{0.2}Ca_{0.2}CoO_{3-\delta}$ (PBSLCC)	LSGM	SFM-GDC|LSGM|PBSLCC	Air/3%H_2O-H_2	1.21 (1073 K) 0.78 (1023 K) 0.46 (973 K)	2023 [13]
NiFe	SSC fiber	LSGM	NiFe|LSGM|SSC	O_2/humid H_2	1.22 (1073 K) 0.83 (1023 K) 0.50 (973 K)	2023 [14]
NiFe	SSC-SDC fiber	LSGM	NiFe|LSGM|SSC-SDC	O_2/humid H_2	1.33 (1073 K) 0.91 (1023 K) 0.57 (973 K)	
$Pr_{0.2}Sr_{0.8}Co_{0.2}Fe_{0.8}O_{3-\delta}$ (PSCF)	PSCF	LSGM	PSCF-GDC|LSGM|PSCF-GDC	Air/humid H_2	0.55 (1073 K) 0.40 (1023 K) 0.20 (973 K)	2024 [15]
NiFe	CeSSC	LSGM	NiFe|TiLDC|LSGM|CeSSC	O_2/humid H_2	**1.20** (1073 K) **0.90** (1023 K) **0.62** (973 K)	This work

Table S5 EC performance at 1.3 V

Anode	Cathode	Electrolyte	Cell structure	Condition	Current Density ($A\ cm^{-2}$)	Ref.
$Sr_2Fe_{1.3}Ni_{0.2}Mo_{0.5}O_6$ (SFMNi)-SDC	LSCF-SDC	LSGM	SFMNi-SDC|LCO|LSGM|SDC-LSCF	Air/42%H_2O-H_2	0.84 (1073 K) 0.51 (1023 K) 0.27 (973 K)	2016 [16]
Ni-YSZ	SSC	LSGM	Ni-YSZ|NiFe|CMF|TiLDC|LSGM|Porous LSGM|SSC	Air/20%H_2O-30%H_2-50% Ar	0.38 (873 K) 0.25 (823 K) 0.13 (773 K)	2020 [17]
$Sr_2Ti_{0.8}Co_{0.2}FeO_6$ (STC02F)	STC02F	LSGM	STC02 F|LSGM|STC02F	Air/50%H_2O-H_2	0.46 (1073 K) 0.37 (1023 K) 0.22 (973 K)	2020 [18]
$La_{0.6}Sr_{0.4}Co_{0.15}Fe_{0.8}Pd_{0.051}O_{3-\delta}$ (LSCFP)	LSCF-GDC	LSGM	LSCFP|LSGM|LSCF-GDC	Air/50%H_2O-H_2	1.62 (1073 K) 1.16 (1023 K) 0.77 (973 K)	2022 [8]
NiO-SDC	$GdBa_{0.5}Sr_{0.5}Co_{0.9}Cu_{1.1}O_{5+\delta}$ (GBSCC)	LSGM	NiO-SDC|LDC|LSGM|GBSCC	Air/humid H_2	0.44 (973 K) 0.34 (923 K) 0.22 (873 K)	2023 [19]
$Sr_2FeCo_{0.5}Mo_{0.5}O_{6-\delta}$ (SFCM)	SFCM	LSGM	SFCM|LDC|LSGM|LDC|SFCM	Air/5%H_2O-N_2	0.32 (973 K) 0.25 (923 K) 0.20 (873 K)	2024 [20]
NiFe	CeSSC	LSGM	NiFe|TiLDC|LSGM|CeSSC	O_2/45%N_2-5%H_2-50H_2O	**0.61** (973 K) **0.36** (923 K) **0.20** (873 K)	This work

References:

[1] G. Zhang, X. Dong, Z. Liu, W. Zhou, Z. Shao, W. Jin, Cobalt-site cerium doped $Sm_xSr_{1-x}CoO_{3-\delta}$ oxides as potential cathode materials for solid-oxide fuel cells, J. Power Source. 195 (2010) 3386-3393.

[2] J.A. Fortner, E.C. Buck, The chemistry of the light rare-earth elements as determined by electron energy loss spectroscopy, Appl. Phys. Lett. 68 (1996) 3817-3819.

[3] W. Yang, H. Zhang, C. Sun, L. Liu, J.A. Alonso, M.T. Fernández-Díaz, L. Chen, Insight into the structure and unctional application of the $Sr_{0.95}Ce_{0.05}CoO_{3-\delta}$ cathode for solid oxide fuel cells, Inorg. Chem. 54 (2015) 3477-3484.

[4] J. Liu, F. Jin, X. Yang, B. Niu, S. Yu, Y. Li, T. He, Synergistic electron doping and ion conductive phase incorporating of $SrCoO_{3-\delta}$ as desirable cathode materials for intermediate-temperature solid oxide fuel cells, Ceram. Int. 46 (2020) 28332-28341.

[5] S. Lee, J.H. Park, K.T. Lee, Y.-W. Ju, Anodic properties of Ni-Fe bimetallic nanofiber for solid oxide fuel cell using $LaGaO_3$ electrolyte, J. Alloy Compound. 875 (2021) 159911.

[6] S.-F. Wang, H.-C. Lu, Y.-F. Hsu, P. Jasinski, High-performance anode-supported solid oxide fuel cells with co-fired $Sm_{0.2}Ce_{0.8}O_{2-\delta}/La_{0.8}Sr_{0.2}Ga_{0.8}Mg_{0.2}O_{3-\delta}/Sm_{0.2}Ce_{0.8}O_{2-\delta}$ sandwiched electrolyte, Int. J. Hydrogen Energ. 47 (2022) 5429-5438.

[7] J. Choi, M. Kim, S.K. Kang, J. Kim, J. Ha, H.H. Shin, T. Park, W.B. Kim, A highly efficient bifunctional electrode fashioned with in situ exsolved NiFe alloys for reversible solid oxide cells, ACS Sustain. Chem. Engin. 10 (2022) 7595-7602.

[8] K.J. Kim, C. Lim, K.T. Bae, J.J. Lee, M.Y. Oh, H.J. Kim, H. Kim, G. Kim, T.H. Shin, J.W. Han, K.T. Lee, Concurrent promotion of phase transition and bimetallic nanocatalyst exsolution in perovskite oxides driven by Pd doping to achieve highly active bifunctional fuel electrodes for reversible solid oxide electrochemical cells, Appl. Catal. B-Environ. 314 (2022) 121517.

[9] F. Li, Y. Xu, Q. Wu, D. Zhao, M. Deng, SOFC cathode material of $La_{1.2}Sr_{0.8}CoO_{4\pm\delta}$ with a fibrous morphology: Preparation and electrochemical performance, International J. Hydrogen Energ. 48 (2023) 3204-3215.
[10] Z. Li, M. Peng, X. Zhang, L. Zhang, J. Li, Y. Sun, Preparation of SOFC anodes at lower temperature with boosted electrochemical performance, ACS Appl. Energy Mater. 6 (2023) 3616-3626.
[11] Q. Zhang, H. Qiu, S. Jiang, Y. Liu, J. Xu, W. Wang, D. Chen, C. Su, Enhanced ORR activity of A-site-deficient $SrCo_{0.8}Nb_{0.1}Ti_{0.1}O_{3-\delta}$ as a bifunctional air electrode for low-temperature solid oxide fuel cells, Energy Fuels, 37 (2023) 6740-6748.
[12] Z. Wang, T. Tan, K. Du, C. Yang, Highly active and stable Cu-Based anode decorated with in situ fabricated CuFe alloy nanoparticles for solid oxide fuel cells, ACS Appl. Energ. Mater. 6 (2023) 6781-6789.
[13] F. He, F. Zhu, D. Liu, Y. Zhou, K. Sasaki, Y. Choi, M. Liu, Y. Chen, A reversible perovskite air electrode for active and durable oxygen reduction and evolution reactions via the A-site entropy engineering, Materials Today, 63 (2023) 89-98.
[14] S.W. Lee, J.-W. Park, Y.-W. Ju, T.H. Shin, Heterogeneous composite fibrous cathode undergoing emphasized active oxygen dissociation for La(Sr)Ga(Mg)O_3-dased high-performed solid oxide fuel cells, Small Structures, 5 (2024) 2300292.
[15] X. Sun, Y. Xia, B. Wang, B. Li, L. Ma, J. Chen, B. Chi, In situ self-reconstructed nanoparticle-coated cathode and anode by nitric acid etching for symmetric solid oxide fuel cells, Chem. Eng. J. 479 (2024) 147598.
[16] Y. Wang, T. Liu, M. Li, C. Xia, B. Zhou, F. Chen, Exsolved Fe–Ni nanoparticles from $Sr_2Fe_{1.3}Ni_{0.2}Mo_{0.5}O_6$ perovskite oxide as a cathode for solid oxide steam electrolysis cells, J. Mater. Chem. A 4 (2016) 14163-14169.
[17] Z. Tan, T. Ishihara, Effect of Ni-based cathodic layer on intermediate temperature tubular electrolysis cell using $LaGaO_3$-based electrolyte thin film, J. Phys.-Energ. 2 (2020) 024004.
[18] B. Niu, C. Lu, W. Yi, S. Luo, X. Li, X. Zhong, X. Zhao, B. Xu, In-situ growth of nanoparticles-decorated double perovskite electrode materials for symmetrical solid oxide cells, Appl. Catal. B-Environ. 270 (2020) 118842.
[19] K. Li, K. Świerczek, P. Winiarz, A. Brzoza-Kos, A. Stępień, Z. Du, Y. Zhang, K. Zheng, K. Cichy, A. Niemczyk, Y. Naumovich, Unveiling the electrocatalytic activity of the $GdBa_{0.5}Sr_{0.5}Co_{2-x}Cu_xO_{5+\delta}$ ($x \geq 1$) oxygen electrodes for solid oxide cells, ACS Appl. Mater. Interface 15 (2023) 39578-39593.
[20] J. Zhao, Y. Shen, J. Gu, Y. Wang, Y. Zhao, Y. Bu, Optimizing water electrolysis activity in Mo-doped $Sr2FeCoO_{6-\delta}$ perovskites by balancing oxygen vacancies and structural stability, J. Power Source 592 (2024) 233928.